

Exotic charge density waves and superconductivity on the Kagome Lattice

Rui-Qing Fu,^{1,2} Jun Zhan,^{3,2} Matteo Dürrnagel,^{4,5} Hendrik Hohmann,⁴ Ronny Thomale,⁴ Jiangping Hu,^{3,6} Ziqiang Wang,^{7,*} Sen Zhou,^{1,2,8,†} and Xianxin Wu^{1,‡}

¹CAS Key Laboratory of Theoretical Physics, Institute of Theoretical Physics, Chinese Academy of Sciences, Beijing 100190, China

²School of Physical Sciences, University of Chinese Academy of Sciences, Beijing 100049, China

³Institute of Physics, Chinese Academy of Sciences, Beijing 100190, China

⁴Institut für Theoretische Physik und Astrophysik, Universität Würzburg, Am Hubland Campus Süd, Würzburg 97074, Germany

⁵Institute for Theoretical Physics, ETH Zürich, 8093 Zürich, Switzerland

⁶New Cornerstone Science Laboratory, Beijing 100190, China

⁷Department of Physics, Boston College, Chestnut Hill, Massachusetts 02467, USA

⁸CAS Center for Excellence in Topological Quantum Computation, University of Chinese Academy of Sciences, Beijing 100049, China

(Dated: May 16, 2024)

Recent experiments have identified fascinating electronic orders in kagome materials, including intriguing superconductivity, charge density wave (CDW) and nematicity. In particular, some experimental evidence for AV_3Sb_5 ($A = K, Rb, Cs$) and related kagome metals hints at the formation of orbital currents in the charge density wave ordered regime, providing a mechanism for spontaneous time-reversal symmetry breaking in the absence of local moments. In this work, we comprehensively explore the competitive charge instabilities of the spinless kagome lattice with inter-site Coulomb interactions at the pure-sublattice van Hove filling. From the analysis of the charge susceptibility, we find that, at the nesting vectors, while the onsite charge order is dramatically suppressed, the bond charge orders are substantially enhanced owing to the sublattice texture on the hexagonal Fermi surface. Furthermore, we demonstrate that nearest-neighbor and next nearest-neighbor bonds are characterized by significant intrinsic real and imaginary bond fluctuations, respectively. The 2×2 loop current order is thus favored by the next nearest-neighbor Coulomb repulsion. Interestingly, increasing interactions further leads to a nematic state with intra-cell sublattice density modulation that breaks the C_6 rotational symmetry. We further explore superconducting orders descending from onsite and bond charge fluctuations, and discuss our model's implications on the experimental status quo.

I. INTRODUCTION

Exploring novel quantum states has been a central theme in contemporary condensed matter physics. As one of its core representatives, electronic correlations have fostered intriguing quantum states in cuprate high-temperature superconductors [1]. In particular, for the pseudogap phase found in the cuprate phase diagram, an exotic charge order with circulating loop currents descending from the marginal Fermi-liquid regime has been proposed by Varma [2, 3]. Such loop current order, which preserves the lattice translational symmetry, is expected to yield unique experimental signatures, and its fluctuations could provide a mechanism for d -wave pairing [2]. Most importantly, the loop current order formation devises a mechanism for correlated electron systems to spontaneously break time reversal symmetry without magnetism, i.e., in the absence of local moments. The experimental status of loop currents in the cuprates, in particular whether they live up to energy scales relevant to high- T_c superconductivity, is still heavily debated [4, 5]. Meanwhile, in theory, the loop current order paradigm has proliferated from the cuprates to bernal-stacked bilayer graphene and twisted bilayer graphene [6, 7], where such proposed orbital loop currents could imply non-trivial topological properties. As fundamentally interesting as

orbital current phases present themselves to be, it has been challenging to theoretically devise a solid microscopic foundation for such a state beyond mean field theory and biased variational methods. This not only applies to the formation of such a state per se, but also to the energy scale associated with it, as already seen by partially conflicting numerical evidence stemming from the analysis of finite size systems [8–12].

The recent discovery of Fermi surface instabilities in kagome materials such as AV_3Sb_5 ($A = K, Rb, Cs$) [13–15] and FeGe [16–18] has unveiled a wealth of remarkable properties, such as intriguing superconductivity (SC) and charge density waves (CDW). In AV_3Sb_5 , the CDW order occurs at a temperature ranging from 78 to 103 K, displaying translational symmetry breaking and $2 \times 2 \times 2$ reconstruction [19, 20]. Intriguingly, signatures of time-reversal symmetry breaking associated with the CDW have been detected through muon spin resonance (μ SR) [21], optical polarization rotation [22], chiral transport [23], magneto-optical Kerr effect measurements [24], and laser-based scanning tunneling microscopy [25]. They imply the potential presence of loop current order in kagome metals with a signal strength and data diversity far beyond existing evidence in cuprates [26–30]. It should be noted, however, that the experimental status quo even for AV_3Sb_5 is far from settled. For instance, high resolution polar Kerr effect studies can be interpreted in favor of the absence of time reversal symmetry breaking [31].

In the kagome metal FeGe, a CDW transition is observed within the A-type antiferromagnetic state [16], where magnetic moments align ferromagnetically within each layer and

* wangzi@bc.edu

† zhousen@itp.ac.cn

‡ xxwu@itp.ac.cn

antiferromagnetically between layers. The CDW shares the same wavevector as observed in AV_3Sb_5 , and its emergence is accompanied with an enhancement in the magnetic moment and anomalous Hall effect [17]. Across these kagome material families, multiple van Hove singularities (VHSs) located near the Fermi level have been identified [32, 33], with the VHSs in FeGe arising from spin-minority bands due to large ferromagnetic splitting in each layer [17, 18]. These VHSs, which exhibit Fermi surface nesting, are believed to play a pivotal role in driving the correlated phenomena observed onsetting to the intra-layer ferromagnetic background, in particular with regard to the CDW.

The VHSs in the kagome lattice exhibit a unique sublattice texture. It implies matrix element reduction effects of scattering channels between VH points, and has hence been coined sublattice interference (SI) [34, 35]. Whenever the accumulation of electronic density of states at the VH points represents a relevant contribution to the formation of Fermi surface instabilities, it is to be expected that SI could have a crucial impact on the nature of electronic order. Despite intensive theoretical studies, the question of whether electronic interactions within the kagome lattice, intertwined with SI, can give rise to loop current states at van Hove filling remains an open issue. Studies using the functional renormalization group approach applied to the t-U-V model have not identified the presence of such orders [34, 36–39]. Mean-field analyses, however, suggest that longer-range interactions, in particular to the range that couples all sites involved in a current loop, could have a crucial impact on loop current order [40]. Additionally, the topological loop current order can get promoted by bond order fluctuations [41].

In this article, we seek to perform model building that aims at providing a microscopic foundation for loop current order. Our work is guided by the core idea that SI in kagome metals could set the stage for loop current order reachable through a full scale many-body analysis beyond mean field and finite size studies. As we delve into the intrinsic charge orders of the kagome lattice, we further reduce complexity by examining a spinless fermionic model with inter-site Coulomb interactions. There are three motivations for this step. First, as we are avoiding complicated magnetic orders via a frozen spin scenario, we can thoroughly study the effect of sublattice texture on charge fluctuations. Second, given the absence of magnetic phases for most kagome metals of our interest, the amount of competing density wave orders removed through this simplification is highly limited, and hence allows to draw rather accurate implications for the spinful model. Third, the model is directly relevant to experiments, like antiferromagnet FeGe. To go beyond mean-field calculations, we employ the random phase approximation (RPA) approach, which allows us to treat both onsite and bond order on equal footing. Our analysis of charge susceptibilities reveals that while the onsite charge order will be suppressed, the bond charge order gets enhanced owing to SI from the sublattice texture associated with the p -type VHS. Moreover, facilitated by the unique lattice's geometry, we observe that the nearest-neighbor (NN) and next NN (NNN) bonds exhibit pronounced intrinsic real and imaginary bond charge fluctuations, respectively. The emergence of a

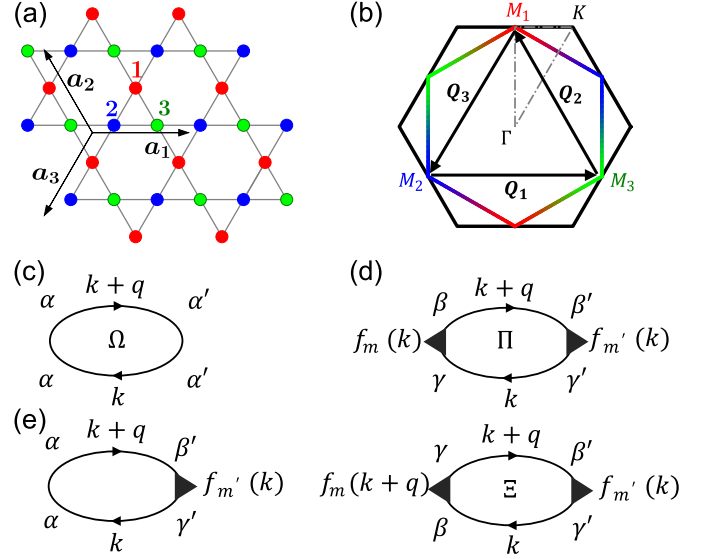


FIG. 1. Kagome lattice and charge susceptibility bubbles. (a) Kagome lattice and (b) the sublattice-resolved Fermi surface at the p -type van Hove filling, with three sublattices indicated by red (1), blue (2) and green (3) circles. The two basis lattice vectors are $\mathbf{a}_1 = (1, 0)$, $\mathbf{a}_2 = (-\frac{1}{2}, \frac{\sqrt{3}}{2})$, with the third vector $\mathbf{a}_3 = -\mathbf{a}_1 - \mathbf{a}_2$. Feynman diagrams for susceptibilities in the onsite (c), bond (d), and mixed (e) channels. Ω is the onsite susceptibility and Π and Ξ are two bond susceptibilities, with $f_m(\mathbf{k})$ describing the corresponding form factors.

2×2 loop current order as the ground state is favored when the NNN repulsion is sufficiently strong, while dominant NN repulsion favors a 2×2 trihexagonal charge bond order and can stabilize a nematic state characterized by charge density modulations within the unit cell. We further explore the nature of triplet superconductivity away from van Hove filling descending from such exotic charge orders within our model, where p - and f -wave pairings emerge due to bond charge fluctuations. Finally, we discuss possible experimental implications and contemplate on future quantitative theoretical studies that build upon the conceptual narrative outlined in our work.

II. TIGHT-BINDING MODEL AND SUSCEPTIBILITIES OF ONSITE AND BOND CHARGE ORDERS

The kagome lattice consists of corner-sharing triangles with three sublattices, as shown in Fig.1(a). The kinetic energy is described by the tight-binding Hamiltonian,

$$\mathcal{H}_0 = -t \sum_{\langle \mathbf{r}\mathbf{r}' \rangle, \alpha \neq \beta} c_\alpha^\dagger(\mathbf{r}) c_\beta(\mathbf{r}') - \mu \sum_{\mathbf{r}\alpha} n_\alpha(\mathbf{r}), \quad (1)$$

where $c_\alpha^\dagger(\mathbf{r})$ and $c_\alpha(\mathbf{r})$ are the creation and annihilation operators of an electron at the lattice site \mathbf{r} , $\alpha = 1, 2, 3$ is the sublattice index, $\langle \mathbf{r}\mathbf{r}' \rangle$ denotes the NN sites, and $n_\alpha(\mathbf{r}) = c_\alpha^\dagger(\mathbf{r}) c_\alpha(\mathbf{r})$ is the electron density operator. t and μ are the NN hopping parameter and chemical potential, respectively. Defining t as

the unit of energy, we set $t = 1$ from now on. The tight-binding band structures feature two VHSs, one Dirac cone, and a flat band. In particular, the Fermi surfaces at the two van Hove (VH) fillings are characterized by distinct sublattice textures [34, 35]. In this work, we focus on the upper VH case at the pristine filling, i.e. the p -type VHS [34, 35], and the sublattice-resolved Fermi surface is displayed in Fig. 1(b). Clearly, the wavefunction at each saddle point (i.e. \mathbf{M} point) is attributed to a single sublattice, while at the midpoint between two saddle points, the wavefunction exhibits a mixture of two sublattices. The Fermi surface nesting vectors $\mathbf{Q}_{1,2,3}$ always connect distinct sublattice characters of states around the three saddle points, leading to substantial bond fluctuations, as will be demonstrated in the subsequent analysis.

To examine the intrinsic fluctuations, we consider the relevant charge orders on the kagome lattice. The first one is charge modulation, i.e., the onsite charge order, and it is described by the operator $n_\alpha(\mathbf{r})$ in real space. In momentum space, this operator reads $n_\alpha(\mathbf{q}) = \frac{1}{\sqrt{N}} \sum_{\mathbf{r}} e^{-i\mathbf{q}\cdot\mathbf{r}} n_\alpha(\mathbf{r}) = \frac{1}{\sqrt{N}} \sum_{\mathbf{k}} c_\alpha^\dagger(\mathbf{k} + \mathbf{q}) c_\alpha(\mathbf{k})$. We additionally consider bond charge modulation, i.e. charge bond order, on NN and NNN bonds. Due to the unique geometry of the kagome lattice, within each unit cell there are two NN (NNN) bonds along the direction parallel (perpendicular) to each basis vector \mathbf{a}_α , and they all connect two distinct sublattices β and γ , with the Levi-civita symbol satisfying $\epsilon_{\alpha\beta\gamma} = 1$, i.e., $(\alpha, \beta, \gamma) = (1, 2, 3), (2, 3, 1),$ and $(3, 1, 2)$. This allows us to define the symmetric (+) and antisymmetric (−) bond operators [30, 40]

$$B_{\alpha,+,\eta}(\mathbf{r}) = \frac{1}{2} \left[c_\beta^\dagger(\mathbf{r}) c_\gamma(\mathbf{r} + \mathbf{l}_{\alpha,\eta}) + c_\beta^\dagger(\mathbf{r}) c_\gamma(\mathbf{r} - \mathbf{l}_{\alpha,\eta}) \right], \quad (2)$$

$$B_{\alpha,-,\eta}(\mathbf{r}) = \frac{i}{2} \left[c_\beta^\dagger(\mathbf{r}) c_\gamma(\mathbf{r} + \mathbf{l}_{\alpha,\eta}) - c_\beta^\dagger(\mathbf{r}) c_\gamma(\mathbf{r} - \mathbf{l}_{\alpha,\eta}) \right], \quad (3)$$

where η denotes NN and NNN bonds, and the corresponding displacement vectors connecting the two sites of β and γ sublattices are $\mathbf{l}_{\alpha,\text{NN}} = \frac{1}{2} \mathbf{a}_\alpha$ and $\mathbf{l}_{\alpha,\text{NNN}} = \frac{1}{2} (\mathbf{a}_\beta - \mathbf{a}_\gamma)$, respectively. Performing Fourier transformation, the bond order operators in the momentum space can be written as,

$$B_{\alpha,\pm,\eta}(\mathbf{q}) = \frac{1}{\sqrt{N}} \sum_{\mathbf{k}} f_{\alpha,\pm,\eta}(\mathbf{k}) c_\beta^\dagger(\mathbf{k} + \mathbf{q}) c_\gamma(\mathbf{k}), \quad (4)$$

with $f_{\alpha,+,\eta}(\mathbf{k}) = \cos(\mathbf{k} \cdot \mathbf{l}_{\alpha,\eta})$ and $f_{\alpha,-,\eta}(\mathbf{k}) = \sin(\mathbf{k} \cdot \mathbf{l}_{\alpha,\eta})$ being the form factors of symmetric and antisymmetric bonds, respectively. We note that the antisymmetric bond defined in this work differs from that in Refs. [30] and [40] by a factor of i , which leads to a real form factor in Eq. (4). Clearly, including NN and NNN bonds, there are in total 12 independent bond orders indexed by (α, \pm, η) within each unit cell. To simplify their indices, we introduce one-dimensional indices $m, n = \{1, 2, \dots, 12\} = \{(1, +, \text{NN}), (1, -, \text{NN}), 1 \rightarrow 2, 3, \text{NN} \rightarrow \text{NNN}\}$. Note that the bond orders are complex in general, we thus introduce their conjugate partners as well, $B_{\alpha,\pm,\eta}^\dagger(\mathbf{r}) \equiv [B_{\alpha,\pm,\eta}(\mathbf{r})]^\dagger$ in real space and, consequently, $[B_{\alpha,\pm,\eta}(\mathbf{q})]^\dagger = B_{\alpha,\pm,\eta}^\dagger(-\mathbf{q})$ in momentum space.

To investigate the intrinsic fluctuations of different charge orders, we calculate the corresponding susceptibilities defined

as,

$$\chi_{pq}(\mathbf{q}, i\omega_n) = \int_0^\beta d\tau e^{i\omega_n \tau} \langle T_\tau O_p(\mathbf{q}, \tau) [O_q(\mathbf{q}, 0)]^\dagger \rangle. \quad (5)$$

Here the operator O_p runs over the 27 charge orders mentioned above, consisting of 24 bond orders in the order of $\{B_1, B_1^\dagger, B_2, B_2^\dagger, \dots, B_{12}, B_{12}^\dagger\}$ followed by the 3 onsite charge orders $\{n_1, n_2, n_3\}$. The bare static susceptibility is given by $\chi_{pq}^0(\mathbf{q}) \equiv \chi_{pq}(\mathbf{q}, 0)$. For the convenience of discussion, we use different notations to distinguish the susceptibilities of onsite and bond charge orders in the following, and we further note that the latter can be categorized into two types. Explicitly, 3×3 susceptibility matrix for onsite charge orders $\Omega_{\alpha\beta}^0 = \chi_{24+\alpha, 24+\beta}^0$, and 24×24 susceptibilities for bond charge orders $\Pi_{mn}^0 = \chi_{2m-1, 2n-1}^0 = \chi_{2m, 2n}^0$ and $\Xi_{mn}^0 = \chi_{2m-1, 2n}^0 = \chi_{2m, 2n-1}^0$ with $m, n = 1, \dots, 12$. The corresponding Feynman diagrams for Ω are just the normal bubbles while those for Π and Ξ carry two additional vertices of form factors, as depicted in Fig. 1(c) and Fig. 1(d). The analytical expressions of Ω , Π , and Ξ are given by

$$\Omega_{\alpha\beta}^0(\mathbf{q}) = -\frac{T}{N} \sum_{\mathbf{k}, l} G_{\beta\alpha}^0(\mathbf{k} + \mathbf{q}, i\omega_l) G_{\alpha\beta}^0(\mathbf{k}, i\omega_l), \quad (6)$$

$$\Pi_{mn}^0(\mathbf{q}) = -\frac{T}{N} \sum_{\mathbf{k}, l} f_m(\mathbf{k}) f_n(\mathbf{k}) \times G_{\beta_n \beta_m}^0(\mathbf{k} + \mathbf{q}, i\omega_l) G_{\gamma_m \gamma_n}^0(\mathbf{k}, i\omega_l), \quad (7)$$

$$\Xi_{mn}^0(\mathbf{q}) = -\frac{T}{N} \sum_{\mathbf{k}, l} f_m(\mathbf{k} + \mathbf{q}) f_n(\mathbf{k}) \times G_{\beta_n \gamma_m}^0(\mathbf{k} + \mathbf{q}, i\omega_l) G_{\beta_m \gamma_n}^0(\mathbf{k}, i\omega_l), \quad (8)$$

where the noninteracting Green's function $G_{\beta\gamma}^0(\mathbf{k}, i\omega_l) = \sum_{\nu} a_{\beta\nu}(\mathbf{k}) a_{\gamma\nu}^*(\mathbf{k}) / (i\omega_l - \epsilon_{\nu\mathbf{k}})$ with $\epsilon_{\nu\mathbf{k}}$ being the ν -th eigen energy of \mathcal{H}_0 and $a_{\beta\nu}(\mathbf{k})$ the corresponding eigen state. The summation over the fermionic Matsubara frequency $\omega_l = (2l+1)\pi k_B T$ at temperature T yields the Lindhard function and sublattice-associated matrix elements with the detailed formulas given in the supplementary material (SM). These sublattice characters embedded in the noninteracting Green's functions play a predominant role in determining the behavior of susceptibilities. The diagram with only one vertex displayed in Fig. 1(e) represents the susceptibility in the mixed channel that couples the onsite and bond charge orders.

Before presenting the numerical data, we analyse the contributions to the bare susceptibilities from the VH points. At the p -type VH filling, the hexagonal Fermi surface encompasses the three inequivalent VH points labeled by $\mathbf{M}_{1,2,3}$ at the zone boundary and features perfect nesting with three wave vectors $\mathbf{Q}_\alpha = \frac{1}{2} \mathbf{G}_\alpha$, where \mathbf{G}_α denotes the reciprocal wave vector of the kagome lattice. These VH points with diverging density of states (DOS) are expected to contribute dominantly to the susceptibilities, especially at the two pertinent vectors, $\mathbf{q} = 0$ and $\mathbf{q} = \mathbf{Q}_\alpha \equiv \mathbf{M}_\alpha$. Furthermore, as mentioned before and shown in Fig. 1(b), the Bloch states at \mathbf{M}_α points are exclusively localized on the α th sublattice. Consequently, the Green's functions at \mathbf{M}_α are non vanishing only for $G_{\alpha\alpha}^0(\mathbf{M}_\alpha)$. It is thus straightforward to show that

these VH points contribute only to the diagonal elements of the onsite charge susceptibilities at $\mathbf{q} = 0$, $\Omega_{\alpha\alpha}(0)$, while their contributions to off-diagonal elements of $\Omega(0)$ and all bond susceptibilities, $\Pi(0)$ and $\Xi(0)$, vanish. This results a dominant onsite charge fluctuation at $\mathbf{q} = 0$. The situation is, however, completely the opposite for wave vector $\mathbf{q} = \mathbf{M}_\alpha$. The two VH points \mathbf{M}_β and \mathbf{M}_γ connected by $\mathbf{q} = \mathbf{Q}_\alpha$ feature pure β th and γ th sublattice, respectively. This feature leads to the vanishing contribution of VH points in the onsite charge fluctuation $\Omega_{\alpha'\alpha''}^0(\mathbf{M}_\alpha)$. But these two VH points can thus dominantly contribute to the susceptibilities $\Pi(\mathbf{M}_\alpha)$ of the bonds that connecting β and γ sublattices. We note that they have no contributions to $\Xi(\mathbf{M}_\alpha)$ since at least one of the two Green's function in Eq. (8) involves mixed sublattices. This indicates predominant bond fluctuations at $\mathbf{q} = \mathbf{M}_\alpha$ rather onsite charge fluctuations. Furthermore, since $\mathbf{M}_{\beta/\gamma} \cdot \mathbf{l}_{\alpha,NN} = \frac{\pi}{2}$ and $\mathbf{M}_{\beta/\gamma} \cdot \mathbf{l}_{\alpha,NNN} = \pm \frac{\pi}{2}$, the contribution from these two VH points to the susceptibilities of symmetric bonds with form factors $\cos(\mathbf{k} \cdot \mathbf{l}_{\alpha,\eta})$ also vanishes. Therefore, at the wave vector $\mathbf{q} = \mathbf{M}_\alpha$, the two connected VH points at \mathbf{M}_β and \mathbf{M}_γ , with $\epsilon_{\alpha\beta\gamma} = 1$, contribute only to the elements of $\Pi(\mathbf{M}_\alpha)$ associated with the antisymmetric bonds that connects β and γ sublattices. Explicitly, taking $\mathbf{q} = \mathbf{M}_1$ as an example, the VH points contribute only to susceptibility $\Pi_{22}(\mathbf{M}_1)$ for bond $B_2 = B_{1,-,NN}$, $\Pi_{88}(\mathbf{M}_1)$ for bond $B_8 = B_{1,-,NNN}$, and $\Pi_{28}(\mathbf{M}_1)$ that couples B_2 and B_8 . Clearly, the unique sublattice texture at the p -type VH filling plays a pivotal role in suppressing the onsite charge fluctuations at wavevector $\mathbf{q} = \mathbf{M}_\alpha$ but significantly promoting the bond charge fluctuations in the antisymmetric channel. This behavior in the kagome lattice markedly differs from what is observed in the triangular and honeycomb lattices, where onsite charge fluctuations are dominant [42, 43]. Additionally, it is readily shown that the contribution from the VH points to the susceptibilities in the mixed channels depicted in Fig. 1(e) vanishes as well at both $\mathbf{q} = 0$ and $\mathbf{q} = \mathbf{M}_\alpha$.

The calculated bare susceptibilities are presented in detail in the SM, with the representative elements displayed in Fig. 2(a) along the high-symmetry path $\Gamma\text{-}\mathbf{M}_1\text{-}\mathbf{K}\text{-}\Gamma$ depicted in Fig. 1(b). A temperature of $k_B T = 0.005$ is applied in the calculation, under which the dominant fluctuations are reflected by the peaks at $\mathbf{q} = 0$ and $\mathbf{q} = \mathbf{M}_\alpha$. Indeed, as suggested by the above analysis of the contribution from the VH points, the diagonal elements of onsite charge susceptibilities $\Omega_{\alpha\alpha}$ dominate at $\mathbf{q} = 0$, while the leading susceptibilities at $\mathbf{q} = \mathbf{M}_1$ are Π_{22} , Π_{88} , and Π_{28} of the antisymmetric bonds connecting the two sites of 2nd and 3rd sublattices. The large $\Pi_{28}^0(\mathbf{M}_1)$ shown in Fig. 2(a) indicates the strong coupling between the NN and NNN antisymmetric bond orders. These results promote the leading fluctuations in the antisymmetric bond channel, instead of symmetric bond or onsite charge channels. However, the nature of the antisymmetric bond order is yet to be explored.

To reveal the nature of the antisymmetric bond order which exhibits the leading fluctuation at the nesting wavevector \mathbf{M}_α , we further separate the bond orders into their real and imagi-

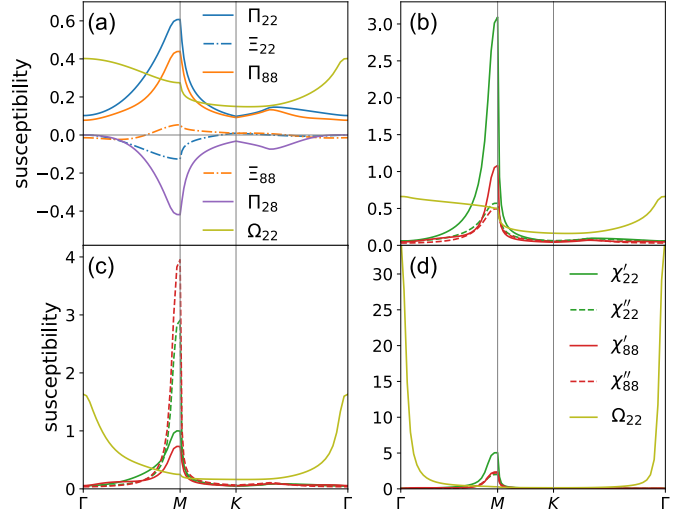


FIG. 2. Bare and RPA susceptibilities along the high-symmetry path. (a) Representative components of the bare susceptibility for onsite and bond charge orders. Representative components of the RPA susceptibilities for onsite and bond charge orders at various inter-site Coulomb interactions: (b) $V_{NN} = 0.6$, $V_{NNN} = 0.0$, (c) $V_{NN} = 0.0$, $V_{NNN} = 0.95$, and (d) $V_{NN} = 0.5$, $V_{NNN} = 0.75$. We adopt $k_B T = 0.005$ in a-c, while a higher temperature $k_B T = 0.01$ in d is used to avoid divergence.

nary parts,

$$B'_m(\mathbf{q}) = \frac{1}{2}[B_m + B_m^\dagger], \quad B''_m(\mathbf{q}) = \frac{1}{2i}[B_m - B_m^\dagger], \quad m \in \text{odd}, \quad (9)$$

$$B'_m(\mathbf{q}) = \frac{1}{2i}[B_m - B_m^\dagger], \quad B''_m(\mathbf{q}) = \frac{1}{2}[B_m + B_m^\dagger], \quad m \in \text{even}. \quad (10)$$

Here the definition in the antisymmetric bond channel is different because of the additional factor i used in Eq. (3). B'_m and B''_m represent the hopping and current modulation on the bonds, respectively. It is straightforward to show that the static susceptibilities of the real and imaginary bond charge orders can be rewritten as,

$$\chi'_{mm}(\mathbf{q}) = [\Pi_{mm}(\mathbf{q}) - (-1)^m \Xi_{mm}(\mathbf{q})]/2, \\ \chi''_{mm}(\mathbf{q}) = [\Pi_{mm}(\mathbf{q}) + (-1)^m \Xi_{mm}(\mathbf{q})]/2. \quad (11)$$

Clearly, the relative strength of real and imaginary bond fluctuations is dictated by the sign of $\Xi(\mathbf{M}_\alpha)$. According to previous line of reasoning, the VH points contribute nothing to Ξ , rendering these fluctuations degenerate when considering only states at VH points. As a result, one has to go *beyond* the VH points and consider the contributions from other portions of the hexagonal FS to determine the sign of $\Xi(\mathbf{M}_\alpha)$.

We consider the diagonal elements of Ξ at $\mathbf{q} = \mathbf{M}_\alpha$ for the antisymmetric bonds connecting β and γ sublattice, i.e., NN bond $B_{2\alpha}$ and NNN bond $B_{6+2\alpha}$, that are tied to the leading fluctuation. Because of the unique geometry of the kagome lattice, the nesting and connecting vectors satisfy $\mathbf{l}_{\alpha,NN} \parallel \mathbf{Q}_\alpha$ and $\mathbf{l}_{\alpha,NNN} \perp \mathbf{Q}_\alpha$, leading to $\mathbf{Q}_\alpha \cdot \mathbf{l}_{\alpha,NN} = \pi$ and

$\mathbf{Q}_\alpha \cdot \mathbf{l}_{\alpha, \text{NNN}} = 0$. Consequently, for \mathbf{k} on the hexagonal FS, the two form factors in $\Xi_{2\alpha, 2\alpha}(\mathbf{Q}_\alpha)$ for the NN antisymmetric bond read $f_{2\alpha}(\mathbf{k} + \mathbf{Q}_\alpha)f_{2\alpha}(\mathbf{k}) = -\sin^2(\mathbf{k} \cdot \mathbf{l}_{\alpha, \text{NN}}) \leq 0$, whereas the two form factors in $\Xi_{6+2\alpha, 6+2\alpha}(\mathbf{Q}_\alpha)$ for the NNN antisymmetric bond are given by $f_{6+2\alpha}(\mathbf{k} + \mathbf{Q}_\alpha)f_{6+2\alpha}(\mathbf{k}) = \sin^2(\mathbf{k} \cdot \mathbf{l}_{\alpha, \text{NNN}}) \geq 0$. These distinctive characteristics suggest that $\Xi_{2\alpha, 2\alpha}(\mathbf{Q}_\alpha)$ and $\Xi_{6+2\alpha, 6+2\alpha}(\mathbf{Q}_\alpha)$ have the opposite signs, pointing to the different nature of bond fluctuations on the NN and NNN bonds. Indeed, as shown in Fig. 1(a), Ξ_{22} is negative while Ξ_{88} is positive at $\mathbf{q} = \mathbf{M}_1$ due to the positive Green's function related sublattice factors. From the Eq. (11), it is apparent that, in the antisymmetric channel, the bare real bond fluctuation on the NN bonds is more pronounced, whereas the bare imaginary bond fluctuation is stronger on the NNN bonds. These distinctive characteristics, determined by the sublattice texture and unique geometry in the kagome lattice, open up the possibility of realizing exotic electronic orders, such as loop current ground states.

III. COMPETING ELECTRONIC STATES WITH INTER-SITE COULOMB INTERACTIONS

To focus on the competition between intrinsic charge orders on the kagome lattice, we consider the simplified spinless model where the spin degree of freedom is removed. In this case, the onsite Coulomb repulsion is absent by the Pauli exclusion and we consider the NN and NNN inter-site Coulomb repulsions,

$$\begin{aligned} \mathcal{H}_{\text{int}} &= \sum_{\eta} V_{\eta} \sum_{\alpha, \mathbf{r}} [n_{\beta}(\mathbf{r})n_{\gamma}(\mathbf{r} + \mathbf{l}_{\eta}) + n_{\beta}(\mathbf{r})n_{\gamma}(\mathbf{r} - \mathbf{l}_{\eta})] \quad (12) \\ &= \frac{1}{N} \sum_{\eta, \alpha} \sum_{\mathbf{k}, \mathbf{k}'} 2V_{\eta}(\mathbf{q})c_{\beta}^{\dagger}(\mathbf{k})c_{\beta}(\mathbf{k} + \mathbf{q})c_{\gamma}^{\dagger}(\mathbf{k}' + \mathbf{q})c_{\gamma}(\mathbf{k}'), \end{aligned}$$

with $V_{\eta}(\mathbf{q}) = V_{\eta} \cos(\mathbf{q} \cdot \mathbf{l}_{\alpha, \eta})$. The interactions can be decoupled in terms of onsite charge orders

$$\mathcal{H}_{\text{int}} = \sum_{\eta, \alpha, \mathbf{q}} 2V_{\eta}(\mathbf{q})[n_{\beta}(\mathbf{q})]^{\dagger} n_{\gamma}(\mathbf{q}), \quad (13)$$

or offsite bond orders

$$\mathcal{H}_{\text{int}} = - \sum_{\eta, \alpha, \mathbf{q}} \sum_{s=\pm} 2V_{\eta}[B_{\alpha, s, \eta}(\mathbf{q})]^{\dagger} B_{\alpha, s, \eta}(\mathbf{q}). \quad (14)$$

Once these interactions are introduced, both onsite and bond charge susceptibilities get renormalized. The first-order ladder of bond susceptibilities can be decomposed into the product of bond susceptibilities in different channels, as the interaction carrying internal momentum of fermion propagators can be decoupled owing to Eq.14, derived from $V_{\eta}(\mathbf{k} - \mathbf{k}') = V_{\eta} \sum_{s=\pm} f_{\alpha, s, \eta}(\mathbf{k})f_{\alpha, s, \eta}(\mathbf{k}')$. The first-order bubble of bond susceptibilities will introduce a susceptibility in the mixed channel with only one vertex (as shown in Fig.1(e)), which is the coupling between bond and onsite charge order. Then, the first-order bubble of this mixed susceptibility will involve the onsite susceptibility. This hierarchy structure can be treated within the susceptibility matrix χ , which involves

both onsite and bond charge orders. We employ the random phase approximation (RPA) summation of all bubble and ladder diagrams (details in SM), that yields the renormalized susceptibility matrix,

$$\chi_{\text{RPA}}(\mathbf{q}) = [1 + \chi^0(\mathbf{q})\mathcal{U}_c(\mathbf{q})]^{-1}\chi^0(\mathbf{q}). \quad (15)$$

The interaction matrix $\mathcal{U}_c(\mathbf{q})$ is given by,

$$\begin{aligned} \mathcal{U}_c(\mathbf{q}) &= \begin{pmatrix} V_{\text{NN}}^c & 0 & 0 \\ 0 & V_{\text{NNN}}^c & 0 \\ 0 & 0 & U^c(\mathbf{q}) \end{pmatrix}, \\ U^c(\mathbf{q}) &= \begin{pmatrix} 0 & V_{12} & V_{13} \\ V_{12} & 0 & V_{23} \\ V_{13} & V_{23} & 0 \end{pmatrix}, \\ V_{\eta}^c &= -\text{diag}\{2V_{\eta}, 2V_{\eta}, \dots\}, \\ V_{\beta\gamma} &= 2V_{\text{NN}}f_{\alpha, +, \text{NN}}(\mathbf{q}) + 2V_{\text{NNN}}f_{\alpha, +, \text{NNN}}(\mathbf{q}), \quad (16) \end{aligned}$$

with the indices α, β, γ being in (α, β, γ) . As the temperature decreases, an eigenvalue of the RPA susceptibility χ_{RPA} at a specific momentum \mathbf{q} turns negative, signaling an instability at this \mathbf{q} vector. The associated eigenvector contains the structure of the charge instability, i.e. the CDW pattern.

According to our previous analysis, the relevant fluctuations are in the onsite and anti-symmetric bond channels and we thus study the effect of inter-site Coulomb interactions on them. With a typical NN repulsion of $V_{\text{NN}} = 0.6$, the susceptibilities in various channels χ''/Ω are displayed in Fig.2(b). The NN bond fluctuations are significantly enhanced at the \mathbf{M} point but the NN real bond susceptibility is dominant, consistent with previous studies [36, 37]. The NN imaginary bond fluctuation (green dashed line) is the subdominant while the onsite charge fluctuation is quite weak. In contrast, with a moderate NNN repulsion $V_{\text{NN}} = 0.95$, the susceptibilities of imaginary bond orders are significant at the \mathbf{M} point and the NNN imaginary bond susceptibility is much larger than the others, as shown in Fig.2(c). This indicates that the NNN repulsion can promote the imaginary bond fluctuation on the NNN bond. When both NN and NNN repulsions are substantial, the onsite charge fluctuation at $\mathbf{q} = \mathbf{0}$ exceeds the bond fluctuations at the \mathbf{M} point and becomes dominant, as shown in Fig.2(d). Meanwhile, the enhancement of the onsite charge susceptibility at the \mathbf{M} point always remains weak, due to the aforementioned sublattice interference effect.

We further scrutinize the eigenvalues of $\chi_{\text{RPA}}(\mathbf{q})$ to study the particle-hole instabilities with decreasing temperature. The obtained phase diagram is displayed in Fig. 3(a), with color representing the transition temperatures. When the NN repulsion is dominant and the NNN repulsion is weak (region I), the susceptibility of real bond order at three \mathbf{M} points first diverges as the temperature decreases and the system favors the charge bond order (CBO). For a dominant NNN repulsion (region II), the imaginary bond order, i.e. loop current order (LCO), is the leading instability. Due to the coupling between bond order on the NN and NNN bonds, both CBO and LCO exhibit a sizable mixture between these bonds, as shown in Fig. 3 (b) and (c). These particle-hole instabilities are consistent with our weak-coupling analysis, which indicates that the real bond order generates uniform larger gaps

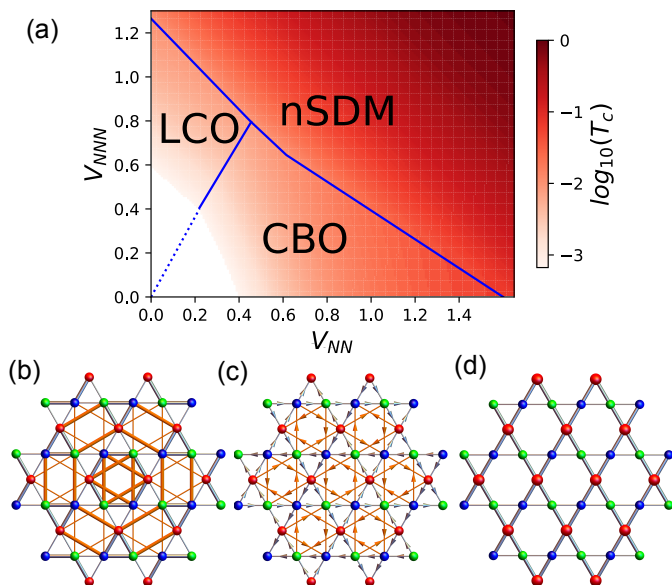


FIG. 3. (a) Phase diagram of the spinless kagome lattice with inter-site Coulomb interactions at the p-type VH filling. Real-space patterns of three orders: (b) trihexagonal pattern of CBO. (c) bond pattern of LCO, (d) nematic CDM. The thick (thin) bond represents a strong (weak) hopping, the arrow represents the direction of current and the size of sphere denotes the charge density. The transition temperature in the white region is below 10^{-3} .

on the Fermi surface for the NN channel and the imaginary bond order produces larger gaps on the Fermi surface for the NNN channel (details in SM). When both NN and NNN repulsions are strong (region III), the two-fold charge order with $\mathbf{q} = 0$ is favored and characterized by a mixture of onsite and symmetric bond orders (shown in Fig. 3 (d)). The onsite order, characterized by distinct occupations on three sublattices, is dubbed as nematic sublattice density modulation (nSDM) and exhibits an electrostatic energy gain that scales linearly with the increasing inter-sublattice repulsion. When the Coulomb repulsion is relatively weak, this energy gain is small and charge bond orders predominate. However, as the repulsion strengthens, the energy benefit of the onsite charge order increases rapidly, making it the dominant configuration under conditions of strong repulsion (details in SM).

For both CBO and LCO, the instability occurs simultaneously at three symmetry related \mathbf{M} points and the ground state can be determined by the analysis of Ginzburg-Landau free energy. In the CBO, the trilinear term favors the triple- \mathbf{M} phase with 2×2 reconstructions and the corresponding sign of its coefficient determines the real-space pattern [29]: a negative sign favors the trihexagonal pattern and a positive sign favors the Star of David pattern. The real-space trihexagonal configuration involving NN and NNN bonds is displayed in Fig.3 (b), where the thick (thin) bond represents a strong (weak) hopping. With typical order parameters, the corresponding unfolded band structure is shown in Fig.4 (a) and the Fermi surface is fully gapped with a maximum gap occurring around the VHSs. For the LCO, the trilinear term van-

ishes due the time-reversal symmetry and the free energy up to quartic terms reads,

$$F_{\text{LCO}} = a\Psi^2 + b\Psi^4 + c(\psi_1^2\psi_2^2 + \psi_2^2\psi_3^2 + \psi_3^2\psi_1^2), \quad (17)$$

where ψ_i is the order parameter of LCO with the vector \mathbf{M}_i and $\Psi^2 = \sum_i \psi_i^2$. The quadratic coefficient is $a = a_0(T - T_c)$ with $a_0 > 0$. The coefficient of the coupling term determines the ground state. A large positive c usually favors the single- \mathbf{M} phase with 1×2 reconstructions but a negative c favors the triple- \mathbf{M} phase with 2×2 reconstructions. Fig.3 (c) illustrates the real-space pattern of triple- \mathbf{M} 2×2 LCO with the six-fold rotational symmetry, where the arrows denote the direction of the current pattern emerging in both NN and NNN bonds. Within this phase, the time-reversal symmetry is broken and the occupied band features a nontrivial Chern number. The unfolded band structure is displayed in Fig.4 (b), and the gap opening is anisotropic: the gap along Γ -K almost vanishes but reaches the maximum at VHSs. Distinct from the CBO, there is an additional state located at the Fermi level around VHSs. These lead to finite spectral weight at the Fermi energy along the Γ -K line and around \mathbf{M} , as observed from the Fermi surface shown in the inset of Fig.4 (b). For the two-fold sublattice density modulation order, the free energy reads,

$$F_{\text{CDW}} = a'(\rho_1^2 + \rho_2^2) + c'(\rho_+^3 + \rho_-^3), \quad (18)$$

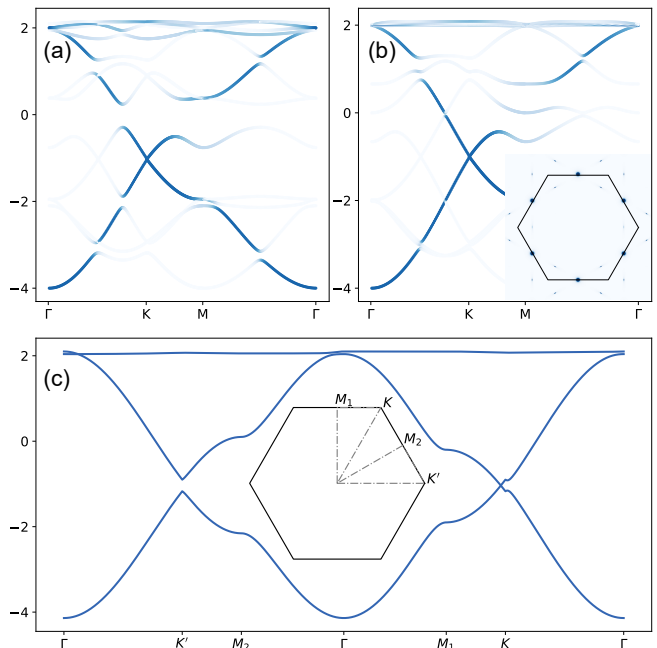


FIG. 4. Unfolded band structure along the high-symmetry path with the 2×2 CBO (a), 2×2 LCO (b) and nematic order with charge density modulations (c). The NN and NNN bond order parameters in the anti-symmetric channel are $\Delta_{-,NN} = -0.12$ and $\Delta_{-,NNN} = 0.07$ for the CBO and $\Delta_{-,NN} = -0.09i$ and $\Delta_{-,NNN} = 0.10i$ for the LCO. For the nematic CDM phase, the adopted parameters are $\Delta_0(2, -1, -1)$ in the onsite channel with $\Delta_0 = 0.1$ and $\Delta_{2(3),+,NN} = 0.05$ in the NN symmetrical channel. The detailed Hamiltonian is provided in SM.

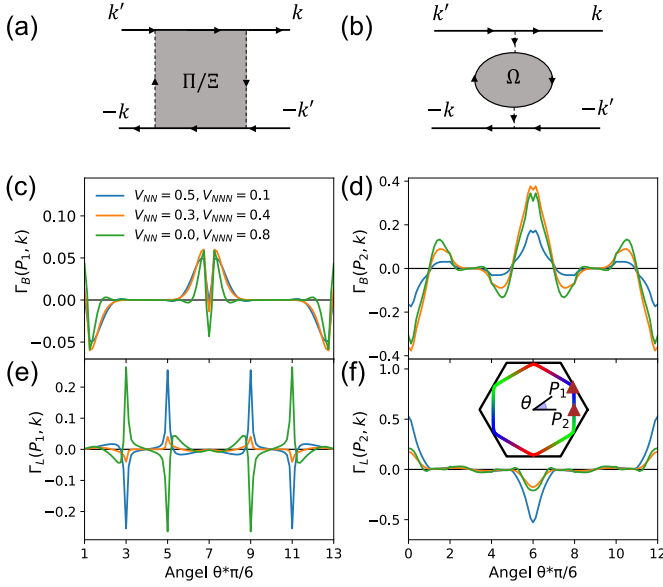


FIG. 5. Effective Cooper pair scattering mediated by onsite and bond charge fluctuations. Feynman diagrams of effective pairing interaction from bond (a) and onsite (b) charge fluctuations. Effective pairing interaction on the Fermi surface from bubbles (c),(d) and ladders (e),(f). Two reference points P_1 and P_2 are marked in the inset of (f) and θ is measured in the counterclockwise direction from the horizontal axis. The adopted chemical potential and temperature are $\mu = 0.01$ and $k_B T = 0.007$, respectively.

where $\rho_{1,2}$ are the two-fold order parameters and $\rho_{\pm} = \rho_1 \pm i\rho_2$. Assuming $(\rho_1, \rho_2) = \rho(\sin 2\theta, \cos 2\theta)$, the cubic term can be written as $\rho^3 \cos(6\theta)$, which is minimized by $2\theta = 2n\pi/3$ for $c' < 0$ and $2\theta = (2n+1)\pi/3$ for $c' > 0$. The resulting order will break the six-fold rotational symmetry and thus is nematic. The order mainly involves charge density modulations within the unit cell and a representative nematic real-space configuration is shown in Fig.3 (d), where the large red spheres denote larger occupation and the red sublattice related bonds have stronger hopping amplitude. As shown in Fig.4 (c), this nSDM order will not introduce any band fold and gap opening around the Fermi level but introduce anisotropic energy shifts for the VHSs.

IV. SUPERCONDUCTIVITY MEDIATED BY ONSITE AND BOND CHARGE DENSITY FLUCTUATIONS

When the Fermi level moves away from VHSs, the Fermi surface nesting weakens, leading to the suppression of both onsite and bond charge orders. However, these charge fluctuations can promote particle-particle instabilities, i.e. superconductivity. In this section, we explore the induced superconducting pairing when these particle-hole orders become unstable. Based on the Feynman diagrams in Fig.5(a) and (b), the onsite charge fluctuation (Ω) peaking at $\mathbf{q} = 0$ dominantly contributes to the forward Cooper pair scattering. While, the bond charge fluctuation (Π/Ξ) peaking at \mathbf{M} points con-

tributes to the Cooper pair scattering with a large momentum transfer. The effective pairing interaction vertex $\Gamma(\mathbf{k}, \mathbf{k}')$ can be expressed as the onsite and bond charge fluctuations in the RPA approximation (details in SM). We tune the chemical potential slightly away from VH filling and the corresponding Fermi surface is shown in the inset of Fig.5(f), where there are two representative points P_1 and P_2 . We plot the effective interaction from RPA bubbles $\Gamma_B(\Omega)$ and ladders $\Gamma_L(\Pi/\Xi)$ with different inter-site Coulomb interactions in Fig.5 (c)-(f), respectively. When one momentum is fixed at the point P_1 , whose eigenvector is dominantly contributed by one sublattice, the effective interaction $\Gamma_B(P_1, \mathbf{k})$ is weak and nonzero only when \mathbf{k} is close to $\pm P_1$ due to the sublattice texture on the Fermi surface [44]. In contrast, the effective interaction $\Gamma_L(P_1, \mathbf{k})$ is substantial and exhibits sharp peaks when \mathbf{k} is in proximity to the other two VHSs. Moreover, the effective interactions display opposite signs in two cases where V_{NN} and V_{NNN} are dominant. The Cooper pair scattering between different VHSs can be exclusively mediated by the bond fluctuation Ξ . The NN and NNN Ξ at the nesting vector features the opposite sign and thus real and imaginary bond fluctuations generate the opposite effective interactions (details in SM), featuring distinct pairing states. When one momentum is fixed at the point P_2 , whose eigenvector is attributed to a mixture of two sublattices, the effective interaction $\Gamma_B(P_2, \mathbf{k})$ is large and peaks at $\mathbf{k} = \pm P_2$. Due to its anti-symmetric nature, it turns repulsive around $\mathbf{k} = -P_2$ ($\theta = \pi$), as indicated from Fig.5 (d). While, the effective interaction $\Gamma_L(P_2, \mathbf{k})$ mainly mediated by the bond fluctuation Π is also significant around $\mathbf{k} = \pm P_2$ and becomes attractive around $\mathbf{k} = -P_2$ but drops to zero when the momentum transfer is large, as shown in Fig.5 (f). Intriguingly, the total effectively interaction $\Gamma_T(P_2, \mathbf{k}) = \Gamma_B(P_2, \mathbf{k}) + \Gamma_L(P_2, \mathbf{k})$ for \mathbf{k} around $-P_2$ is attractive with a dominant V_{NN} but repulsive with a dominant V_{NNN} , which determines the pairing gap functions.

Near the transition temperature, the gap function can be obtained by solving the linearized gap equation,

$$-\int_{\text{FS}} \frac{\sqrt{3}d\mathbf{k}'}{2(2\pi)^2|v_{\mathbf{k}'|}} V^t(\mathbf{k}, \mathbf{k}') \Delta_i(\mathbf{k}') = \lambda_i \Delta_i(\mathbf{k}), \quad (19)$$

where $v_F(\mathbf{k})$ is the Fermi velocity at the momentum \mathbf{k} on the Fermi surface (FS). λ_i denotes the pairing strength for the gap function $\Delta_i(\mathbf{k})$ from the pairing interaction vertex in the triplet (t) channel, with $V^t(\mathbf{k}, \mathbf{k}') = \frac{1}{2}[\Gamma_T(\mathbf{k}, \mathbf{k}') - \Gamma_T(\mathbf{k}, -\mathbf{k}')] (for details see SM). We study the dominant pairing states based on the above equation and Fig.6 (a) displays the leading pairing eigenvalues with a variation of V_{NNN} and a fixed $V_{NN} = 0.2$. The p -wave state is favored for $V_{NNN} < 0.2$. For an intermediate V_{NNN} , the $f_{x^3-3xy^2}$ -wave pairing is dominant. Increasing V_{NNN} further, the eigenvalue of the $f_{y^3-3yx^2}$ -wave pairing increases rapidly and becomes the leading around $V_{NNN} = 1.0$. The comprehensive $V_{NN} - V_{NNN}$ phase diagram is illustrated in Fig.6 (c). Here, the two dominant p -wave and $f_{x^3-3xy^2}$ -wave pairings lie adjacent to CBO and LCO/nSDM, implying that their emergence are facilitated by the corresponding charge fluctuations. The corresponding gap functions are displayed in the Fig.6 (c)-(e), where the f -wave gaps feature a sign change with a six-fold rotation and $p_{x,y}$ -wave state is$

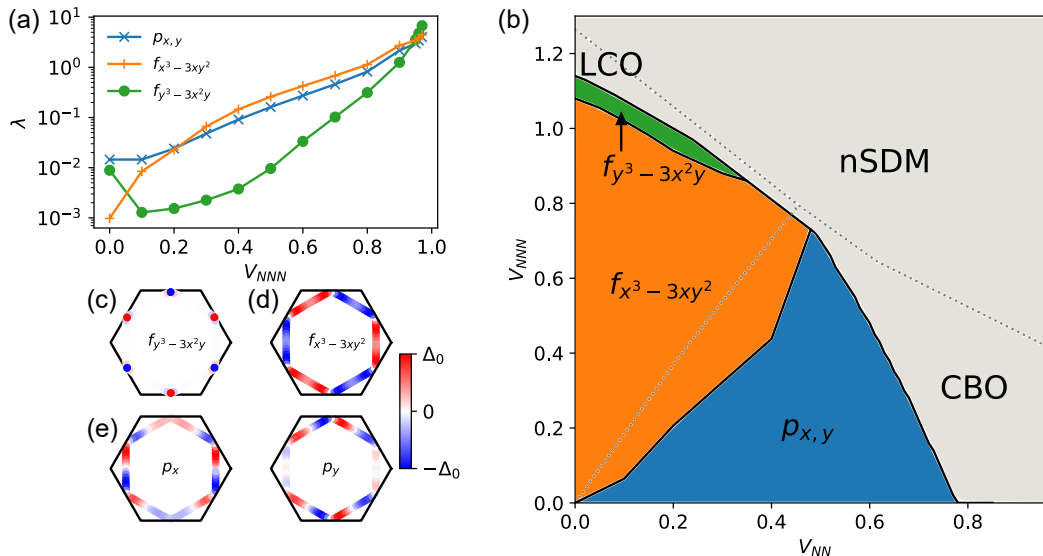


FIG. 6. Superconducting phase diagram and leading gap functions away from the p-type VH filling. (a) Pairing eigenvalues λ with a variation of V_{NNN} and a fixed $V_{NN} = 0.2$. (b) Phase diagram of superconductivity from the inter-site repulsions. In upper right region, RPA charge susceptibilities diverge at the adopted temperature $k_B T = 0.007$ and thus particle-hole instabilities are leading. Representative superconducting gap functions: (c) $f_{y^3-3x^2y}$ -wave (d) $f_{x^3-3xy^2}$ -wave (e) p -wave.

two-fold degenerate. The $p_{x,y}$ -wave pairing tends to form a $p_x + ip_y$ state to maximize the superconducting condensation energy. The $f_{y^3-3xy^2}$ -wave state existing in a narrow region is extremely close to LCO, indicating that it is dominantly promoted by loop current fluctuations. The superconducting gaps around saddle points connected by the nesting vectors have same sign, which is dictated by the attractive pairing interaction between different VHSs. The $f_{x^3-3xy^2}$ -wave pairing is generated by both LCO and nSDM fluctuations and the sign-reversed gaps between two opposite edges are attributed to the repulsive nature of $\Gamma_T(P_2, \mathbf{k})$ around $\mathbf{k} = -P_2$. The p -wave pairing is driven by the CBO fluctuations and the attractive total interaction $\Gamma_T(P_2, \mathbf{k})$ around $\mathbf{k} = -P_2$ ensures that the gaps maintains the same sign on two opposite edges. In addition, its odd-parity nature will introduce line nodes along Γ -K line.

V. DISCUSSIONS AND CONCLUSIONS

At the p-type VH filling, the associated sublattice texture on the Fermi surface plays pivotal role in determining the correlated states in the kagome lattice. The real-space 2×2 modulated onsite charge order is significantly suppressed and the bond charge order gets promoted due to the sublattice interference. Owing to the unique geometry of the kagome lattice, the NN and NNN bonds are characterized by strong intrinsic real and imaginary bond fluctuations, respectively. The loop current state can naturally emerge when there is a strong NNN repulsion. Our work demonstrates that the kagome lattice is an ideal platform to realize such loop current state. The obtained 2×2 loop current order is in the anti-symmetric channel and breaks the translational symmetry derived from the Fermi

surface nesting. It is distinct from the loop current order in the symmetric channel with $\mathbf{q} = 0$ at $1/3$ or $2/3$ fillings, where quadratic band touching is believed to be essential [45–47].

In the nonmagnetic kagome materials, there is an additional degree of freedom, i.e. electron's spin. In a spinful model, the onsite Coulomb repulsion becomes relevant and the onsite charge fluctuation gets enhanced as the charge density doubles. A strong NNN repulsion will further enhance the onsite CDW, rendering the LCO subleading. However, the third NN repulsion acting on the same sublattice can suppress the CDW and LCO may still be stabilized in certain parameter space. A strong onsite Coulomb interaction can enhance the spin bond order and complicates the phase diagram, which deserves future investigation.

We discuss the potential experimental implications of the correlated states in our calculations. The obtained 2×2 LCO state can be relevant in two types of kagome materials. In AV_3Sb_5 , the CDW exhibits an in-plane 2×2 reconstruction and time-reversal symmetry breaking. There are both p-type and m-type VHSs in the vicinity of the Fermi level and the multi-orbital nature and strong hybridization between V d orbitals and Sb p orbitals can enhance the inter-site repulsion in the kagome lattice [32, 33]. These are consistent with our setting in our model calculations. Moreover, the multiple types of VHSs may be helpful to stabilize LCO in the spinful case [48]. The CDW observed in AV_3Sb_5 may be attributed to the LCO and driven by inter-site Coulomb interactions. Another relevant kagome material is FeGe, which exhibits both antiferromagnetic and CDW orders. Each kagome layer is ferromagnetic and ferromagnetic splitting is large, resulting multiple spin-polarized VHSs in proximity to the Fermi level [17, 18]. This spin-polarized band is close to the adopted spinless kagome model here. The orbital mag-

netism associated with LCO can account for the change of magnetic moment upon the CDW transition in FeGe [17, 18]. The nematic SDM involving onsite and symmetric bond orders in our calculations can account for the nematicity in CsTi₃Bi₅ observed by the quasi-particle interference in STM measurements [49, 50]. Especially, the observed anisotropic symmetry-breaking feature in momentum space can be attributed to the nematic bond order.

In summary, our study demonstrates that the loop current state can be stabilized within the spinless kagome lattice, driven by the pronounced imaginary bond fluctuations on next-nearest-neighbor (NNN) bonds. The uncovered sublattice texture plays a pivotal role in the formation of bond charge orders, with the accompanying sublattice interference being deeply connected to the emergence of exotic correlated states. Our findings shed light on the unique character of the kagome lattice and propose a new mechanism for realizing exotic orders in kagome-based materials, such as loop current states.

VI. ACKNOWLEDGMENTS

R.F., S.Z., and X.W. are supported by the National Key R&D Program of China (Grants No. 2023YFA1407300 and

2022YFA1403800) and the National Natural Science Foundation of China (Grants No. 12374153, 12047503, and 11974362). J.Z. and J.P. are supported by the Ministry of Science and Technology (Grant No. 2022YFA1403901), the National Natural Science Foundation of China (Grant No. NSFC-11888101), and the New Cornerstone Investigator Program. Z.W. is supported by U.S. Department of Energy, Basic Energy Sciences Grant No. DE-FG02-99ER45747 and the Cottrell SEED Award No. 27856 from Research Corporation for Science Advancement. R.T., M.D. and H.H. acknowledge funding by the Deutsche Forschungsgemeinschaft (DFG, German Research Foundation) through Project-ID 258499086 - SFB 1170, and through the research unit QUAST, FOR 5249, project ID 449872909, and through the Würzburg-Dresden Cluster of Excellence on Complexity and Topology in Quantum Matter – ct.qmat Project-ID 390858490- EXC 2147. Numerical calculations in this work were performed on the HPC Cluster of ITP-CAS.

-
- [1] P. A. Lee, N. Nagaosa, and X.-G. Wen, Doping a mott insulator: Physics of high-temperature superconductivity, *Rev. Mod. Phys.* **78**, 17 (2006).
- [2] C. M. Varma, Non-fermi-liquid states and pairing instability of a general model of copper oxide metals, *Phys. Rev. B* **55**, 14554 (1997).
- [3] C. M. Varma, Pseudogap phase and the quantum-critical point in copper-oxide metals, *Phys. Rev. Lett.* **83**, 3538 (1999).
- [4] P. Bourges, D. Bounoua, and Y. Sidis, Loop currents in quantum matter, *Comptes Rendus. Physique* **22**, 7 (2021).
- [5] T. P. Croft, E. Blackburn, J. Kulda, R. Liang, D. A. Bonn, W. N. Hardy, and S. M. Hayden, No evidence for orbital loop currents in charge-ordered yb_acu₃o_{6+x} from polarized neutron diffraction, *Phys. Rev. B* **96**, 214504 (2017).
- [6] L. Zhu, V. Aji, and C. M. Varma, Ordered loop current states in bilayer graphene, *Phys. Rev. B* **87**, 035427 (2013).
- [7] N. Bultinck, E. Khalaf, S. Liu, S. Chatterjee, A. Vishwanath, and M. P. Zaletel, Ground state and hidden symmetry of magic-angle graphene at even integer filling, *Phys. Rev. X* **10**, 031034 (2020).
- [8] C. Weber, A. Läuchli, F. Mila, and T. Giamarchi, Orbital currents in extended hubbard models of high- T_c cuprate superconductors, *Phys. Rev. Lett.* **102**, 017005 (2009).
- [9] M. Greiter and R. Thomale, No evidence for spontaneous orbital currents in numerical studies of three-band models for the cuo planes of high temperature superconductors, *Phys. Rev. Lett.* **99**, 027005 (2007).
- [10] R. Thomale and M. Greiter, Numerical analysis of three-band models for cuo planes as candidates for a spontaneous t-violating orbital current phase, *Phys. Rev. B* **77**, 094511 (2008).
- [11] C. Weber, T. Giamarchi, and C. M. Varma, Phase diagram of a three-orbital model for high- T_c cuprate superconductors, *Phys. Rev. Lett.* **112**, 117001 (2014).
- [12] Y. F. Kung, C.-C. Chen, B. Moritz, S. Johnston, R. Thomale, and T. P. Devereaux, Numerical exploration of spontaneous broken symmetries in multiorbital hubbard models, *Phys. Rev. B* **90**, 224507 (2014).
- [13] B. R. Ortiz, L. C. Gomes, J. R. Morey, M. Winiarski, M. Bordelon, J. S. Mangum, I. W. H. Oswald, J. A. Rodriguez-Rivera, J. R. Neilson, S. D. Wilson, E. Ertekin, T. M. McQueen, and E. S. Toberer, New kagome prototype materials: discovery of kv₃sb₅, rbv₃sb₅, and csv₃sb₅, *Phys. Rev. Materials* **3**, 094407 (2019).
- [14] T. Neupert, M. M. Denner, J.-X. Yin, R. Thomale, and M. Z. Hasan, Charge order and superconductivity in kagome materials, *Nature Physics* **18**, 137 (2022).
- [15] K. Jiang, T. Wu, J.-X. Yin, Z. Wang, M. Z. Hasan, S. D. Wilson, X. Chen, and J. Hu, Kagome superconductors av₃sb₅ (a=k, rb, cs) (2021).
- [16] J.-X. Yin, Y.-X. Jiang, X. Teng, M. S. Hossain, S. Mardanya, T.-R. Chang, Z. Ye, G. Xu, M. M. Denner, T. Neupert, B. Lienhard, H.-B. Deng, C. Setty, Q. Si, G. Chang, Z. Guguchia, B. Gao, N. Shumiya, Q. Zhang, T. A. Cochran, D. Multer, M. Yi, P. Dai, and M. Z. Hasan, Discovery of charge order and corresponding edge state in kagome magnet fege, *Phys. Rev. Lett.* **129**, 166401 (2022).
- [17] X. Teng, L. Chen, F. Ye, E. Rosenberg, Z. Liu, J.-X. Yin, Y.-X. Jiang, J. S. Oh, M. Z. Hasan, K. J. Neubauer, B. Gao, Y. Xie, M. Hashimoto, D. Lu, C. Jozwiak, A. Bostwick, E. Rotenberg, R. J. Birgeneau, J.-H. Chu, M. Yi, and P. Dai, Discovery of charge density wave in a kagome lattice antiferromagnet, *Nature* **609**, 490 (2022).
- [18] X. Teng, J. S. Oh, H. Tan, L. Chen, J. Huang, B. Gao, J.-X. Yin, J.-H. Chu, M. Hashimoto, D. Lu, C. Jozwiak, A. Bost-

- wick, E. Rotenberg, G. E. Granroth, B. Yan, R. J. Birgeneau, P. Dai, and M. Yi, Magnetism and charge density wave order in kagome fege, *Nature Physics* **19**, 814 (2023).
- [19] Y.-X. Jiang, J.-X. Yin, M. M. Denner, N. Shumiya, B. R. Ortiz, G. Xu, Z. Guguchia, J. He, M. S. Hossain, X. Liu, J. Ruff, L. Kautzsch, S. S. Zhang, G. Chang, I. Belopolski, Q. Zhang, T. A. Cochran, D. Multer, M. Litskevich, Z.-J. Cheng, X. P. Yang, Z. Wang, R. Thomale, T. Neupert, S. D. Wilson, and M. Z. Hasan, Unconventional chiral charge order in kagome superconductor kv3sb5, *Nature Materials* **20**, 1353 (2021).
- [20] Z. Liang, X. Hou, F. Zhang, W. Ma, P. Wu, Z. Zhang, F. Yu, J.-J. Ying, K. Jiang, L. Shan, Z. Wang, and X.-H. Chen, Three-dimensional charge density wave and surface-dependent vortex-core states in a kagome superconductor csv₃sb₅, *Phys. Rev. X* **11**, 031026 (2021).
- [21] C. Mielke, D. Das, J. X. Yin, H. Liu, R. Gupta, Y. X. Jiang, M. Medarde, X. Wu, H. C. Lei, J. Chang, P. Dai, Q. Si, H. Miao, R. Thomale, T. Neupert, Y. Shi, R. Khasanov, M. Z. Hasan, H. Luetkens, and Z. Guguchia, Time-reversal symmetry-breaking charge order in a kagome superconductor, *Nature* **602**, 245 (2022).
- [22] Q. Wu, Z. X. Wang, Q. M. Liu, R. S. Li, S. X. Xu, Q. W. Yin, C. S. Gong, Z. J. Tu, H. C. Lei, T. Dong, and N. L. Wang, Revealing the immediate formation of two-fold rotation symmetry in charge-density-wave state of Kagome superconductor CsV₃Sb₅ by optical polarization rotation measurement, arXiv e-prints, arXiv:2110.11306 (2021), arXiv:2110.11306 [cond-mat.supr-con].
- [23] C. Guo, C. Putzke, S. Konyzheva, X. Huang, M. Gutierrez-Amigo, I. Errea, D. Chen, M. G. Vergniory, C. Felser, M. H. Fischer, T. Neupert, and P. J. W. Moll, Switchable chiral transport in charge-ordered kagome metal csv3sb5, *Nature* **611**, 461 (2022).
- [24] Y. Xu, Z. Ni, Y. Liu, B. R. Ortiz, S. D. Wilson, B. Yan, L. Balents, and L. Wu, Universal three-state nematicity and magneto-optical Kerr effect in the charge density waves in AV₃Sb₅ (A=Cs, Rb, K), arXiv e-prints, arXiv:2204.10116 (2022), arXiv:2204.10116 [cond-mat.str-el].
- [25] Y. Xing, S. Bae, E. Ritz, F. Yang, T. Birol, A. N. C. Salinas, B. R. Ortiz, S. D. Wilson, Z. Wang, R. M. Fernandes, and V. Madhavan, Optical manipulation of the charge density wave state in rbv3sb5 (2024), arXiv:2308.04128 [cond-mat.str-el].
- [26] X. Feng, K. Jiang, Z. Wang, and J. Hu, Chiral flux phase in the kagome superconductor av3sb5, *Science Bulletin* **66**, 1384 (2021).
- [27] M. M. Denner, R. Thomale, and T. Neupert, Analysis of charge order in the kagome metal av₃sb₅ ($a = \text{K, Rb, Cs}$), *Phys. Rev. Lett.* **127**, 217601 (2021).
- [28] Y.-P. Lin and R. M. Nandkishore, Complex charge density waves at van hove singularity on hexagonal lattices: Haldane-model phase diagram and potential realization in the kagome metals aV₃sb₅ ($a=\text{k, rb, cs}$), *Phys. Rev. B* **104**, 045122 (2021).
- [29] T. Park, M. Ye, and L. Balents, Electronic instabilities of kagome metals: Saddle points and landau theory, *Phys. Rev. B* **104**, 035142 (2021).
- [30] S. Zhou and Z. Wang, Chern fermi pocket, topological pair density wave, and charge-4e and charge-6e superconductivity in kagomé superconductors, *Nature Communications* **13**, 7288 (2022).
- [31] D. R. Saykin, C. Farhang, E. D. Kountz, D. Chen, B. R. Ortiz, C. Shekhar, C. Felser, S. D. Wilson, R. Thomale, J. Xia, and A. Kapitulnik, High resolution polar kerr effect studies of csv₃sb₅: Tests for time-reversal symmetry breaking below the charge-order transition, *Phys. Rev. Lett.* **131**, 016901 (2023).
- [32] Y. Hu, X. Wu, B. R. Ortiz, S. Ju, X. Han, J. Ma, N. C. Plumb, M. Radovic, R. Thomale, S. D. Wilson, A. P. Schnyder, and M. Shi, Rich nature of van hove singularities in kagome superconductor csv3sb5, *Nature Communications* **13**, 2220 (2022).
- [33] M. Kang, S. Fang, J.-K. Kim, B. R. Ortiz, S. H. Ryu, J. Kim, J. Yoo, G. Sangiovanni, D. Di Sante, B.-G. Park, C. Jozwiak, A. Bostwick, E. Rotenberg, E. Kaxiras, S. D. Wilson, J.-H. Park, and R. Comin, Twofold van hove singularity and origin of charge order in topological kagome superconductor csv3sb5, *Nature Physics* **18**, 301 (2022).
- [34] M. L. Kiesel and R. Thomale, Sublattice interference in the kagome hubbard model, *Phys. Rev. B* **86**, 121105 (2012).
- [35] X. Wu, T. Schwemmer, T. Müller, A. Consiglio, G. Sangiovanni, D. Di Sante, Y. Iqbal, W. Hanke, A. P. Schnyder, M. M. Denner, M. H. Fischer, T. Neupert, and R. Thomale, Nature of unconventional pairing in the kagome superconductors av₃sb₅ ($a = \text{K, Rb, Cs}$), *Phys. Rev. Lett.* **127**, 177001 (2021).
- [36] W.-S. Wang, Z.-Z. Li, Y.-Y. Xiang, and Q.-H. Wang, Competing electronic orders on kagome lattices at van hove filling, *Phys. Rev. B* **87**, 115135 (2013).
- [37] M. L. Kiesel, C. Platt, and R. Thomale, Unconventional fermi surface instabilities in the kagome hubbard model, *Phys. Rev. Lett.* **110**, 126405 (2013).
- [38] Y.-Q. Liu, Y.-B. Liu, W.-S. Wang, D. Wang, and Q.-H. Wang, Electronic orders on the kagome lattice at the lower van hove filling, *Phys. Rev. B* **109**, 075127 (2024).
- [39] J. B. Profe, L. Klebl, F. Grandi, H. Hohmann, M. Dürnagel, T. Schwemmer, R. Thomale, and D. M. Kennes, The kagome Hubbard model from a functional renormalization group perspective, arXiv e-prints, arXiv:2402.11916 (2024), arXiv:2402.11916 [cond-mat.str-el].
- [40] J.-W. Dong, Z. Wang, and S. Zhou, Loop-current charge density wave driven by long-range coulomb repulsion on the kagomé lattice, *Phys. Rev. B* **107**, 045127 (2023).
- [41] R. Tazai, Y. Yamakawa, and H. Kontani, Charge-loop current order and z3 nematicity mediated by bond order fluctuations in kagome metals, *Nature Communications* **14**, 7845 (2023).
- [42] S.-J. O, Y.-H. Kim, O.-G. Pak, K.-H. Jong, C.-W. Ri, and H.-C. Pak, Competing electronic orders on a heavily doped honeycomb lattice with enhanced exchange coupling, *Phys. Rev. B* **103**, 235150 (2021).
- [43] N. Gneist, D. Kiese, R. Henkel, R. Thomale, L. Classen, and M. M. Scherer, Functional renormalization of spinless triangular-lattice fermions: N-patch vs. truncated-unity scheme, *The European Physical Journal B* **95**, 157 (2022).
- [44] X. Wu, D. Chakraborty, A. P. Schnyder, and A. Greco, Crossover between electron-electron and electron-phonon mediated pairing on the kagome lattice, *Phys. Rev. B* **109**, 014517 (2024).
- [45] K. Sun, H. Yao, E. Fradkin, and S. A. Kivelson, Topological insulators and nematic phases from spontaneous symmetry breaking in 2d fermi systems with a quadratic band crossing, *Phys. Rev. Lett.* **103**, 046811 (2009).
- [46] J. Wen, A. Rüegg, C.-C. J. Wang, and G. A. Fiete, Interaction-driven topological insulators on the kagome and the decorated honeycomb lattices, *Phys. Rev. B* **82**, 075125 (2010).
- [47] W. Zhu, S.-S. Gong, T.-S. Zeng, L. Fu, and D. N. Sheng, Interaction-driven spontaneous quantum hall effect on a kagome lattice, *Phys. Rev. Lett.* **117**, 096402 (2016).
- [48] H. Li, Y. B. Kim, and H.-Y. Kee, Intertwined van-Hove Singularities as a Mechanism for Loop Current Order in Kagome Metals, arXiv e-prints, arXiv:2309.03288 (2023), arXiv:2309.03288 [cond-mat.str-el].

- [49] H. Yang, Y. Ye, Z. Zhao, J. Liu, X.-W. Yi, Y. Zhang, J. Shi, J.-Y. You, Z. Huang, B. Wang, J. Wang, H. Guo, X. Lin, C. Shen, W. Zhou, H. Chen, X. Dong, G. Su, Z. Wang, and H.-J. Gao, Superconductivity and orbital-selective nematic order in a new titanium-based kagome metal CsTi₃Bi₅, [arXiv e-prints](#), arXiv:2211.12264 (2022), arXiv:2211.12264 [cond-mat.supr-[con](#)].
- [50] H. Li, S. Cheng, B. R. Ortiz, H. Tan, D. Werhahn, K. Zeng, D. Johrendt, B. Yan, Z. Wang, S. D. Wilson, and I. Zeljkovic, Electronic nematicity without charge density waves in titanium-based kagome metal, [Nature Physics](#) **19**, 1591 (2023).